Nano Research
2024, 17(5): 3667–3674

ISSN 1998-0124 CN 11-5974/O4
https://doi.org/10.1007/s12274-023-6262-1

Research Article

Organic ligand nanoarchitectonics for $BiVO_4$ photoanodes surface passivation and cocatalyst grafting

Jingyi Lin[1,2], Xin Li[3], Zhiliang Wang[2], Runlu Liu[1], Hui Pan[1,4], Yixin Zhao[3], Lingti Kong[1], Yao Li[1], Shenmin Zhu[1] (✉), and Lianzhou Wang[2] (✉)

[1] *State Key Laboratory of Metal Matrix Composites, School of Materials Science and Engineering, Shanghai Jiao Tong University, Shanghai 200240, China*
[2] *Nanomaterials Centre, School of Chemical Engineering and Australian Institute for Bioengineering and Nanotechnology, the University of Queensland, QLD 4072, Australia*
[3] *School of Environmental Science and Engineering, Shanghai Jiao Tong University, Shanghai 200240, China*
[4] *Hubei Key Laboratory of Plasma Chemistry and Advanced Materials, Wuhan Institute of Technology, Wuhan 430205, China*

Received: 11 September 2023 / **Revised:** 9 October 2023 / **Accepted:** 11 October 2023

ABSTRACT

Bismuth vanadate ($BiVO_4$) is a promising photoanode material for efficient photoelectrochemical (PEC) water splitting, whereas its performance is inhibited by detrimental surface states. To solve the problem, herein, a low-cost organic molecule 1,3,5-benzenetricarboxylic acid (BTC) is selected for surface passivation of $BiVO_4$ photoanodes (BVOs), which also provides bonding sites for Co^{2+} to anchor, resulting in a Co-BTC-BVO photoanode. Owing to its strong coordination with metal ions, BTC not only passivates surface states of BVO, but also provides bonding between BVO and catalytic active sites (Co^{2+}) to form a molecular cocatalyst. Computational study and interfacial charge kinetic investigation reveal that chemical bonding formed at the interface greatly suppresses charge recombination and accelerates charge transfer. The obtained Co-BTC-BVO photoanode exhibits a photocurrent density of 4.82 mA/cm^2 at 1.23 V vs. reversible hydrogen electrode (RHE) and a low onset potential of 0.22 V_{RHE} under AM 1.5 G illumination, which ranks among the best photoanodes coupled with Co-based cocatalysts. This work presents a novel selection of passivation layers and emphasizes the significance of interfacial chemical bonding for the construction of efficient photoanodes.

KEYWORDS

bismuth vanadate, photoanode, water splitting, surface passivation, bridging ligands

1 Introduction

Photoelectrochemical (PEC) water splitting is a sustainable solar energy utilization strategy for hydrogen energy production [1–3]. The core of a PEC system is semiconductive photoelectrodes that capture solar energy and drive oxidation or reduction reactions to release O_2 or H_2 [4], therefore, the properties of semiconductors determine the overall efficiency of a PEC system [5]. Among all the semiconductor materials, bismuth vanadate ($BiVO_4$) is one of the most promising n-type semiconductors for photoanodes because of its suitable band gap of ~ 2.4 eV and favorable band edge position [4]. Theoretically, the maximum photocurrent density of $BiVO_4$ is about 7.5 mA/cm^2 under AM 1.5 G illumination. However, the inevitable presence of surface trapping states, which originate from surface defects, causes severe electron-hole recombination and the unfavorable surface reaction kinetics [6–8]. Therefore, the experimental outcomes of $BiVO_4$ are inhibited.

As is known, loading cocatalysts is an efficient strategy to improve performance, but additional recombination centers may also form at the semiconductor/cocatalyst interface due to the sharp interruption of crystal structure [9–11]. Passivation interlayers (e.g., Al_2O_3 [9], TiO_2 [12], and CoO_x [8]) are widely introduced to suppress interfacial charge recombination and the pinning of Fermi level. But their processing is highly dependent on some costly techniques (e.g., atomic layer deposition), and these interlayers may shade light absorption of semiconductors [6]. Therefore, it's quite challenging to find a novel and low-cost strategy for photoanode surface passivation.

Passivation with small molecules has been reported for some photoelectrodes [13, 14], which is supposed to be a potential alternative. Small molecules can passivate surface states through chemisorption to dangling bonds and have high transparency. Smith et al. reported that borate species bonded with Bi atoms alter the electronic property of semiconductor and lead to the passivation of surface states [15], thus alleviated charge recombination was observed. However, the studies of small molecule passivated $BiVO_4$ photoanode are quite limited. Because of the large ionic radius (1.31 Å) and complex coordination geometry of Bi^{3+}, only very few kinds of small molecules can coordinate with Bi^{3+} and form stable complex [16]. Among them, 1,3,5-benzenetricarboxylic acid (BTC) is the only inexpensive organic reagent, and BiBTC metal-organic framework (MOF) was reported as a photocatalyst [17] and electrocatalyst [18].

Address correspondence to Shenmin Zhu, smzhu@sjtu.edu.cn; Lianzhou Wang, l.wang@uq.edu.au

清華大學出版社 Tsinghua University Press Springer

What's more, surface decoration with special chemical moieties can also construct a transition layer without severe lattice discontinuity. Active species for oxygen evolution reaction (OER) (e.g., Co^{2+}) can be directly linked to $BiVO_4$ by organic molecules, consequently reducing the thickness of cocatalysts to molecular level and avoiding the formation of a sharp interface [19]. Sun et al. [20] reported a molecular cocatalyst assembled with Co^{2+} and cucurbituril, which possessed mono-molecular layer thickness and high activity. Based on these, BTC may also act as a promising "bridge" molecule between $BiVO_4$ and Co^{2+} for passivated surface states and cocatalyst loading simultaneously.

Herein, BTC is successfully coated onto $BiVO_4$ (BVO) photoanodes through a solvothermal reaction. The BTC-decorated BVO (BTC-BVO) exhibits enhanced performance for both water oxidation reaction and sulfite oxidation reaction because of the passivated surface. Upon loading Co^{2+}, BTC molecules act as a bridge between BVO and Co^{2+}, leading to the formation of an efficient and conformal molecular cocatalyst. As a result of surface passivation and enhanced charge transfer induced by the organic linker BTC, the photocurrent density of Co-BTC-BVO can be promoted to 4.82 mA/cm^2 at 1.23 V_{RHE} (RHE: reversible hydrogen electrode) with a low onset potential of 0.22 V_{RHE} under AM 1.5 G illumination, which surpasses most $BiVO_4$ photoanodes with Co-based cocatalysts.

2 Results and discussion

2.1 Structural and compositional characterization of BTC-decorated $BiVO_4$

BVO electrodes were first synthesized through a previously-reported method [21]. Then, the BVO electrodes were subjected to solvothermal treatment in a solution of 0.05 M BTC (Fig. 1(a), details in Section 4). The obtained samples were denoted as BTC-BVO. Detailed investigations were carried out to figure out the structural and compositional changes during the treatment. After the treatment, X-ray diffraction (XRD) pattern and Raman spectrum of BTC-BVO show no additional peak or obvious peak shift compared with that of untreated BVO (Fig. 1(b) and Fig. S1 in the Electronic Supplementary Material (ESM)), implying that the crystalline phase and structure remain unchanged. As shown in scanning electron microscopy (SEM) images, the BTC-BVO sample remains nanoporous morphology after the solvothermal treatment, the same as pure BVO (Fig. 1(c) and Fig. S2 in the ESM). The lattice spacing of BTC-BVO in high-resolution transmission electron microscopy (HRTEM) image is 0.46 nm, which can be assigned to the (110) plane of monoclinic $BiVO_4$ (Fig. 1(d)). Therefore, the BTC treatment applied here does not result in detectable structural and morphological changes in bulk $BiVO_4$.

Chemical composition of BTC-BVO was then investigated. EDS images in Fig. 1(e) prove the uniform distribution of C element on the surface of $BiVO_4$ particles. However, no obvious amorphous layer can be observed in HRTEM image in Fig. 1(d), suggesting the molecular-level passivation [20]. FTIR spectrum is more sensitive to a trace amount of organic molecules. As shown in Fig. 1(f), several new peaks appear after BTC coating. The peaks at 1363, 1431, and 1545 cm^{-1} can be assigned to the symmetric and asymmetric vibration of C–O in BTC, and the peak at 1607 cm^{-1} corresponds to stretching vibration of C–C [22]. The Fourier transform infrared (FTIR) spectra clearly reveal that BTC molecules are successfully anchored onto BVO. Furthermore, high-resolution XPS spectra of C 1s in Fig. S3 in the ESM can be deconvoluted into three peaks at 288.0, 285.1, and 284.5 eV, assigned to C=O, C–O, and C–C, respectively. Compared to BVO electrode, the relative areas of both C=O and C–O peaks increase in BTC-BVO (Table S1 in the ESM), which is consistent with FTIR results. Therefore, after treatment, a molecular-level BTC layer is successfully coated onto the $BiVO_4$ surface.

The chemical interaction between BTC and BVO is proved by

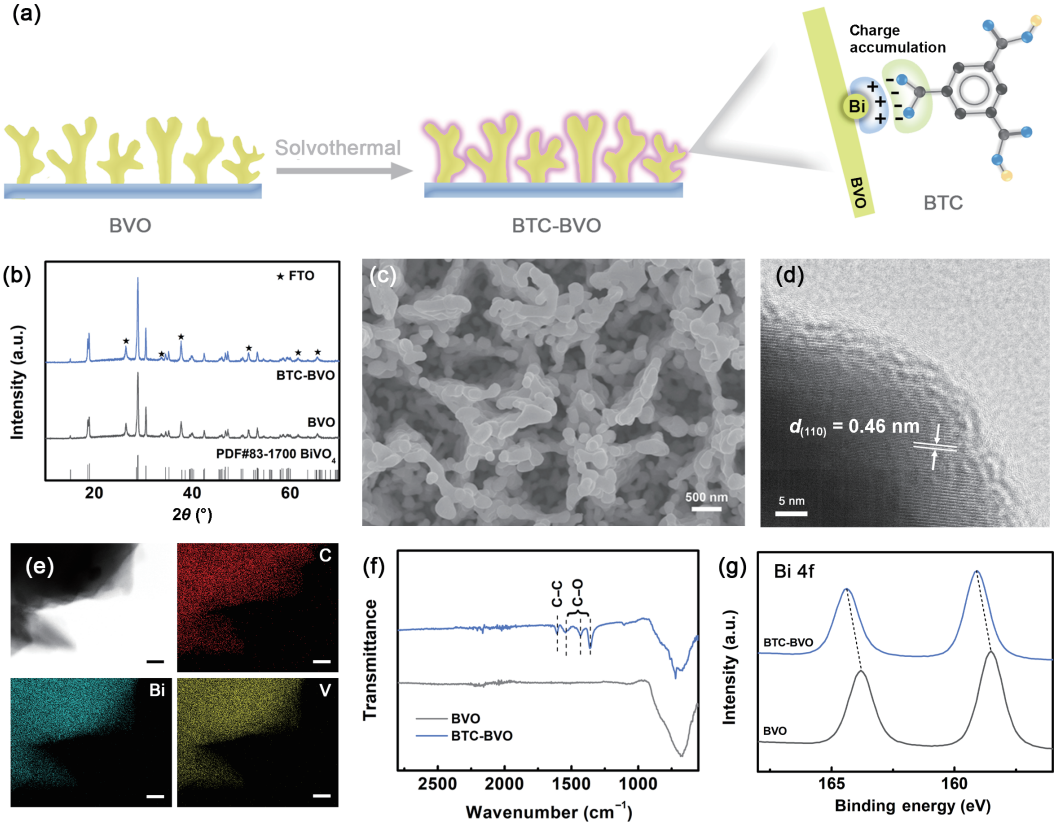

Figure 1 (a) Schematic illustration of BTC treatment of BVO photoanode. (b) XRD patterns of BVO and BTC-BVO photoanodes. (c) SEM image and (d) HRTEM image of BTC-BVO. (e) EDS mappings of BTC-BVO. Scale bar: 20 nm. (f) FTIR spectra and (g) high-resolution Bi 4f XPS spectra of BVO and BTC-BVO.

the shift to higher binding energy in the high-resolution XPS Bi 4f peaks of BTC-BVO [23, 24], as shown in Fig. 1(g). The strong interaction was further studied by density functional theory (DFT) calculation. Three-dimensional (3D) charge density difference in Fig. S4 in the ESM clearly unveils that electron density increases at the BTC side and decreases at the BVO side, which is consistent with XPS peak shift of Bi in Fig. 1(g). Furthermore, the electron accumulation around the carboxyl group suggests its enhanced conjugation effect, resulting in a strong coordination between BTC and BVO [25]. Therefore, BTC molecules are successfully coated onto BVO through chemical bonding, which may also be beneficial to charge transfer.

2.2 PEC performances of BTC-BVO

The water oxidation reaction (WOR) performance of BVO and BTC-BVO electrodes was measured in 1 M potassium borate solution (1 M KBi, pH = 9.7). Obvious performance enhancement after BTC passivation can be observed. As the solid lines in Fig. 2(a) show, the photocurrent density of BTC-BVO at 1.23 V vs. RHE is 2.49 mA/cm^2, about 1.67-fold of the pristine BVO photoanode (1.50 mA/cm^2). The applied bias photon-to-current efficiency (ABPE) is calculated as given in Fig. S5 in the ESM. The highest ABPE of BVO is 0.20% at 0.98 V_{RHE}, while BTC-BVO exhibits a maximum ABPE of 0.47% at a lower potential (0.85 V_{RHE}). Meanwhile, the incident photon-to-current conversion efficiency (IPCE) test also exhibits an obvious enhancement after the BTC treatment. The IPCE values of pristine BVO photoanode are lower than 30% within the whole measured range. By contrast, the maximum IPCE value of BTC-BVO is 52% at 380 nm (Fig. 2(b)). The BTC-BVO photoanode also shows stable H_2 and O_2 gas production at 0.8 V_{RHE}. As shown in Fig. 2(c), the gas evolution fits well with the calculated values, and the Faradaic efficiency is over 90%, thus the photogenerated charge carriers participate in water splitting reaction efficiently.

The sulfite oxidation reaction (SOR) performance was also measured in 1 M KBi electrolyte with 0.2 M Na_2SO_3 (dash lines in Fig. 2(a)). The photocurrent densities of BTC-BVO and BVO are 5.51 and 3.99 mA/cm^2 at 1.23 V_{RHE}, respectively. As listed in Table S2 in the ESM, the performances of BTC-BVO are superior to most of $BiVO_4$ photoanodes without cocatalysts for both WOR and SOR reactions. Therefore, the performance enhancement of $BiVO_4$ photoanodes is achieved by a low-cost and facile BTC treatment, which may be a new strategy for photoanode design.

The light absorption properties of two photoanodes were first investigated. According to ultraviolet–visible (UV–Vis) spectra and the Tauc plots in Fig. S6 in the ESM, two photoanodes show similar absorption edge and the band gap of 2.50 eV, which is consistent with the light absorption edge of 500 nm in IPCE curves (Fig. 2(b)). The light absorption efficiency was calculated accordingly, as given in Fig. 2(d). It is found that BTC-BVO photoanode only shows a slight light absorption enhancement compared to BVO when the wavelength is larger than 500 nm, which may result from the absorption of BTC molecules. But the light absorption region of $BiVO_4$ is lower than 500 nm, where BTC passivation layer has high transparency and will not block out light harvesting of semiconductor.

Assuming that the absorbed photons are completely converted into electrons, the theoretical maximum photocurrent densities of BTC-BVO and BVO can be calculated by integrating the light absorptance-wavelength curves with standard solar spectrum (Eq. S(2) in the ESM). The J_{abs} of BTC-BVO and BVO photoanodes are 6.12 and 5.90 mA/cm^2, respectively. Subsequently, charge separation and transfer efficiencies can also be calculated. As shown in Fig. 2(e), η_{sep} of BTC-BVO is about 90.0% at 1.23 V_{RHE}, while pristine BVO only shows a η_{sep} of 67.6%, and the charge transfer efficiency η_{trans} of BTC-BVO is also higher than BVO electrode (Fig. 2(f)). Mott–Schottky (M–S) analysis in Fig. S7 in the ESM shows both two photoanodes have n-type characteristics and similar carrier densities, so the bulk property is unchanged. Therefore, we suppose that the decoration of BTC mainly has an impact on the surface property, and the promoted charge behavior originates from surface passivation of $BiVO_4$ because the decoration of BTC reduces surface states [26, 27].

2.3 Passivation effect of BTC

The surface passivation effect of BTC is proven by steady-state photoluminescence (PL) spectra and time-resolved photoluminescence (TRPL) decay spectra. As shown in Fig. 3(a), the PL intensity of BTC-BVO is lower than that of pristine BVO photoanode, indicating the enhanced photogenerated carrier separation and lower recombination rate. Furthermore, the TRPL decay curves given in Fig. 3(b) are fitted by a biexponential function. As listed in Table S3 in the ESM, the fitted parameters τ_1 and τ_2 can be attributed to electron-hole pair recombination on the surface and in the bulk [28], which are both increased after BTC treatment. The calculated average lifetime $<\tau>$ of BTC-BVO

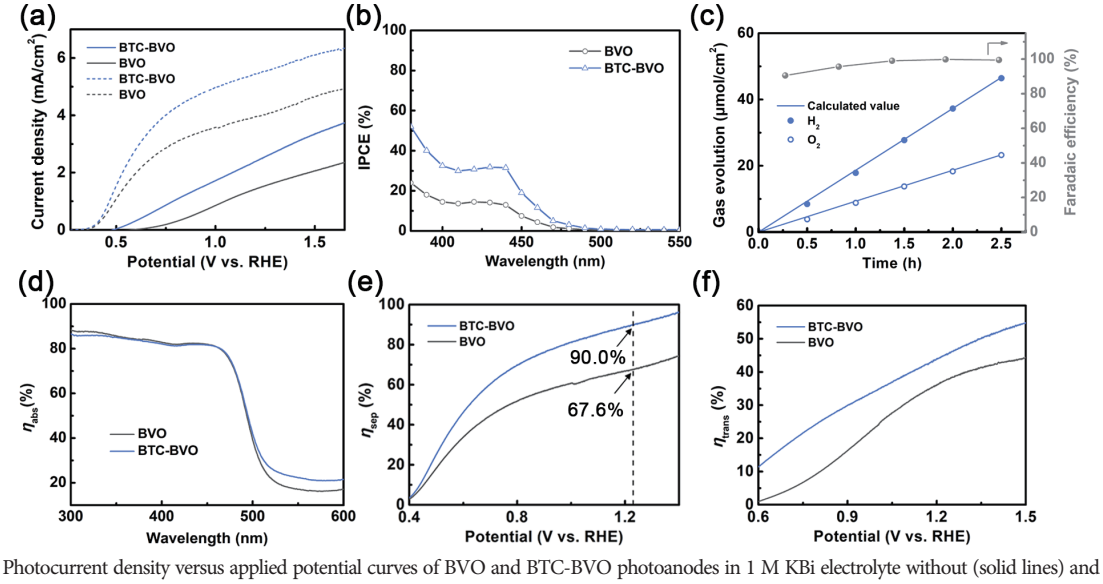

Figure 2 (a) Photocurrent density versus applied potential curves of BVO and BTC-BVO photoanodes in 1 M KBi electrolyte without (solid lines) and with Na_2SO_3 (dash lines). (b) IPCE curves of BVO and BTC-BVO photoanodes. (c) Gas evolution of BTC-BVO at 0.8 V vs. RHE. (d) Light absorption efficiency, (e) charge separation efficiency, and (f) charge transfer efficiency of BVO and BTC-BVO photoanodes.

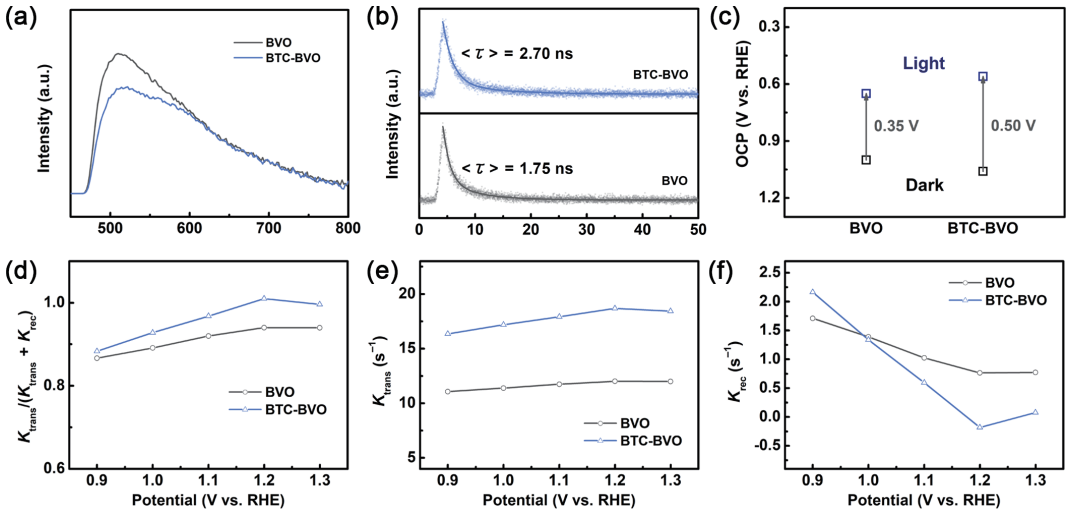

Figure 3 (a) PL spectra and (b) TRPL decay spectra of BVO and BTC-BVO. (c) OCP under dark and light condition. (d) Charge transfer efficiencies, (e) charge transfer rate constants, and (f) charge recombination rate constants of BVO and BTC-BVO extracted from IMPS spectra.

photoanode is 2.70 ns, considerably longer than that of BVO (1.75 ns), which indicates that lower recombination rate of BTC-BVO prolongs the lifetime of charge carriers. The decreased PL intensity and longer lifetime strongly suggest the passivation of surface defects of $BiVO_4$ [29].

Furthermore, the passivation of BVO is confirmed by the open-circuit potential (OCP) curves under chopped illumination, given in Fig. S8 in the ESM. The values of OCP after reaching steady-state equilibrium are summarized in Fig. 3(c). Mismatch between OCP under dark condition and water oxidation potential (1.23 V_{RHE}) is a result of the presence of surface defects [4], thus higher dark OCP of BTC-BVO suggests the reduction of surface states. The difference between OCPs under dark and illuminated condition reflects the degree of band bending at the semiconductor/electrolyte interface [30, 31]. The ΔOCP of BTC-BVO is about 0.50 V, higher than that of pristine BVO (0.35 V), which also indicates steeper band bending and higher photovoltage due to the surface passivation.

The promoted interfacial charge transfer dynamics owing to the surface passivation were investigated by intensity-modulated photocurrent spectroscopy (IMPS). Figure S9 in the ESM demonstrates typical IMPS responses of BVO and BTC-BVO photoanodes at varying applied potentials from 0.9 to 1.3 V_{RHE}. Each IMPS curve consists of two semicircles in the first and fourth quadrants of the complex plane with two intercepts on the real axis [32]. The calculated charge transfer efficiency $K_{trans}/(K_{trans} + K_{rec})$ from the IMPS curves (Fig. 3(d)) proves that charge transfer is improved in BTC-BVO photoanode, which agrees with the tendency of η_{trans} calculated from LSV curves in Fig. 2(f). Charge transfer rate constant (K_{trans}) can also be calculated from the IMPS spectra, as given in Fig. 3(e). BTC-BVO photoanode exhibits higher K_{trans} than bare BVO photoanode. Electrochemical impedance spectroscopy (EIS) spectra in Fig. S10 in the ESM also prove the enhanced charge transfer. The semicircle of the spectrum of BTC-BVO is much smaller than that of BVO. EIS curves were then fitted using the equivalent circuit inset, and the parameters are listed in Table S4 in the ESM. The charge transfer resistance R_{ct} of BTC-BVO is only 19.563 kΩ, much lower than that of BVO (662.11 kΩ).

As is known, at the low-frequency region in the first quadrant, IMPS process is dominated by minor carriers, representing the hole recombination process [33]. As shown in Fig. S9 in the ESM, smaller semicircles can be observed in the first quadrant for BTC-BVO photoanode, and the calculated charge recombination rate constant (K_{rec}) of BTC-BVO in Fig. 3(f) is obviously lower than that of BVO, which indicates that charge recombination is effectively inhibited. Therefore, all the spectroscopic results from IMPS and EIS verify that after the BTC passivation, photogenerated holes transfer across the semiconductor/electrolyte interface more easily with the charge recombination suppressed.

Based on the above analysis, it can be stated that BTC can passivate surface states of $BiVO_4$ without blocking its light absorption. As a result, the charge recombination is suppressed, and charge transfers across the semiconductor/electrolyte interface more easily. Therefore, enhanced WOR and SOR performances of BTC-BVO are observed due to the promoted interfacial charge behavior.

2.4 Enhanced performance of BTC-BVO with Co^{2+}

To further improve the surface OER kinetics, reaction-active species cobalt ions were introduced onto the photoanodes. The as-prepared BTC-BVO photoanodes were soaked in the Co^{2+} solution, denoted as Co-BTC-BVO. The immersion time was optimized to obtain the best performance (Fig. S11 in the ESM). As previously reported, transition metal ions can chelate with carboxyl groups easily [23], thus BTC molecules can assist in the uniform distribution of Co^{2+} and serve as a "bridge" between BVO and Co ions. As shown in Fig. S11 in the ESM, the photocurrent density reaches the maximum after 10 min immersion and shows no further improvement with longer immersion, suggesting that the coordination is saturated. What's more, the formed cocatalyst Co-BTC with the molecular-level thickness is supposed to have high atomic utilization and ultrashort carrier diffusion distance. To verify our hypothesis, photoanodes without BTC transition layer were prepared (denoted as Co-BVO). BVO photoanodes coupled with bulk CoBTC cocatalyst (denoted as (CoBTC)-BVO) were also prepared by a modified solvothermal method, in which the precursors of Co^{2+} and BTC were added in the meantime (details in Section 4). The preparation procedures for three samples are sketched in Fig. 4(a).

High-resolution Co 2p XPS spectrum of Co-BTC-BVO (Fig. S12(a) in the ESM) is composed of two main peaks and two satellite peaks. The Co $2p_{3/2}$ peak at 780.8 eV can be assigned to Co^{2+}. Moreover, compared to BTC-BVO, the C=O and C–O peaks in XPS C 1s spectra of Co-BTC-BVO shift close to each other by 0.10 eV (Fig. S12(b) in the ESM). Therefore, Co^{2+} is adsorbed by carboxyl groups instead of forming oxides or (oxy)hydroxides [20]. The morphology of these samples was examined by SEM. As shown in Figs. 4(b) and 4(c), both Co-BTC-

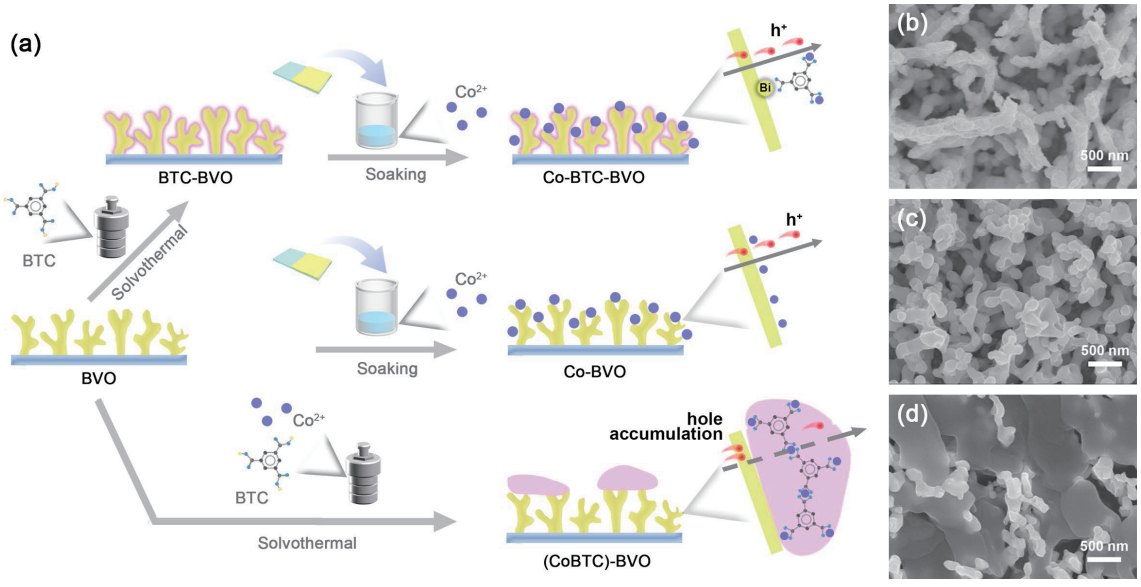

Figure 4 (a) Schematic illustration of the preparation and chemical bonding nature of Co-BTC-BVO, Co-BVO and (CoBTC)-BVO. SEM images of (b) Co-BTC-BVO, (c) Co-BVO, and (d) (CoBTC)-BVO.

BVO and Co-BVO remain in the nanoporous structure of the original BVO photoanodes without obvious aggregation of nanoparticles, indicating that Co ions distribute uniformly on the nanoparticles. By contrast, as shown in Fig. 4(d), $BiVO_4$ is covered by irregular nanosheets in (CoBTC)-BVO, which should be bulk CoBTC MOF. Since the precursors of Co^{2+} and BTC are added together, CoBTC MOF tends to form first through the solvothermal reaction and then attach onto $BiVO_4$. However, due to the low content, the XRD patterns of all three photoanodes in Fig. S13 in the ESM only show diffraction peaks of monoclinic $BiVO_4$ and the FTO substrate.

The Co species greatly enhances the OER performance of BTC-BVO. As shown in Fig. 5(a), the photocurrent density of Co-BTC-BVO reaches 4.82 mA/cm^2 at 1.23 V_{RHE} under AM 1.5 G illumination. Both Co-BVO and (CoBTC)-BVO show lower performance than Co-BTC-BVO. As shown in Fig. 5(a), the photocurrent density at 1.23 V_{RHE} of Co-BVO is about 3.49 mA/cm^2, while that of (CoBTC)-BVO is merely 3.08 mA/cm^2. The *J*–*V* curve of Co-BTC-BVO has a more convex shape with an onset potential of about 0.22 V. Compared to BTC-BVO and bare BVO (Fig. 2(a)), there are negative shifts of about 270 and 390 mV, respectively. The low onset potential exhibits the outstanding activity of the novel molecular cocatalyst, thus endowing Co-BTC-BVO photoanode a maximum ABPE of 1.61% at 0.64 V_{RHE} (Fig. 5(b)). As listed in Table S5 in the ESM, combined photocurrent density and onset potential, the performance of molecular-cocatalyst coupled Co-BTC-BVO is superior to most reported $BiVO_4$ photoanodes coupled with Co-based cocatalysts. Our Co-BTC molecular cocatalyst has better performance than that of bulk cocatalysts, such as CoO_x [34] and CoBi [35], attributing to interfacial chemical bonds formed and the suppressed charge recombination. Since a PEC cell prefers photoanodes with more convex *J*–*V* curves [36], the Co-BTC-BVO photoanode reported here may be a promising candidate for device assembly.

IPCE curves in Fig. 5(c) also prove the excellent performance of Co-BTC-BVO. The highest IPCE value of Co-BTC-BVO is approaching 90%, while (CoBTC)-BVO shows the lowest IPCE value below 60%. What's more, the IPCE curves demonstrate that three photoanodes have similar absorption edges of 500 nm, consistent to the band gap of 2.50 eV. UV–Vis spectra in Fig. S14 in the ESM also show that they possess similar light absorption

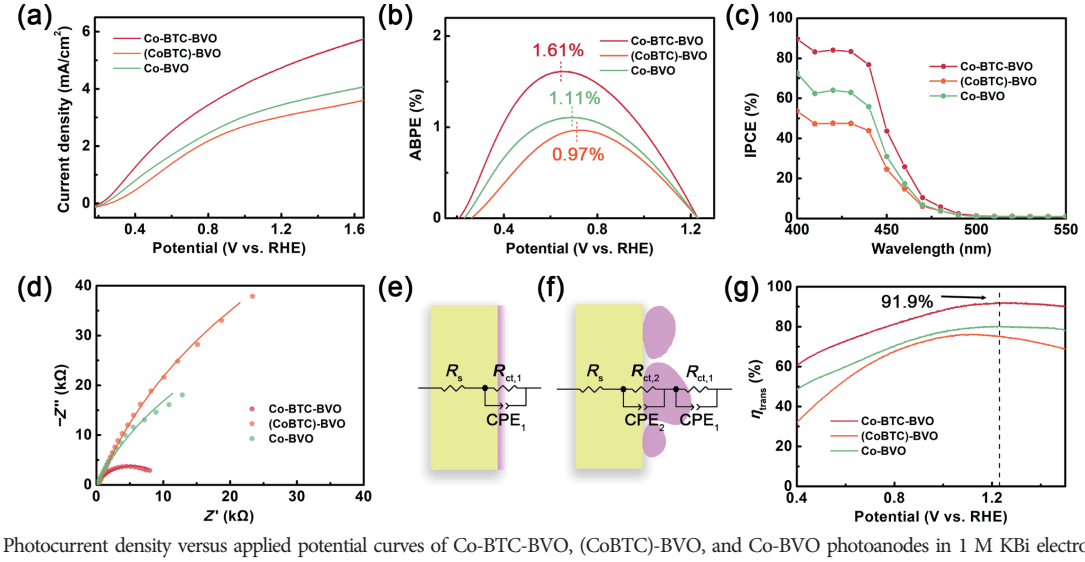

Figure 5 (a) Photocurrent density versus applied potential curves of Co-BTC-BVO, (CoBTC)-BVO, and Co-BVO photoanodes in 1 M KBi electrolyte. (b) ABPE curves, (c) IPCE curves, and (d) EIS spectra of Co-BTC-BVO, (CoBTC)-BVO, and Co-BVO photoanodes. (e) Schematic diagram of interfacial model and equivalent circuit model for Co-BTC-BVO, Co-BVO, and (f) (CoBTC)-BVO. (g) Charge transfer efficiency curves.

property. Therefore, different cocatalyst coating methods do not result in the change of light absorption.

Charge behavior at the semiconductor/cocatalyst interface is the main reason for this performance difference, which is investigated by EIS. As shown in Fig. 5(d), (CoBTC)-BVO photoanode exhibits the largest semicircle, corresponding to the highest charge transfer resistance, while Co-BTC-BVO has the smallest semicircle and charge transfer resistance. The EIS spectra are quantitatively analyzed by equivalent circuit models that describe the charge movement and accumulation in the system [37]. In these models, the resistor R_s is series resistance, and the interface where charge accumulation occurs can be represented by RC element with resistor and constant phase element (CPE) in parallel [38]. The impedance of a CPE is expressed as $Z_{CPE} = \frac{1}{T(j\omega)^P}$ [39, 40]. If CPE-P is close to 1, then its behavior is more similar with a capacitor [41].

According to the fitting results, both Co-BTC-BVO and Co-BVO can be well-fitted by a typical Randles circuit (Fig. 5(e)). Nevertheless, the Randles circuit is not suitable for the EIS spectrum of (CoBTC)-BVO, therefore another circuit model with two RC elements is applied instead to decrease error, as given in Fig. 5(f). The fitted results are listed in Table S6 in the ESM. Because of the branched nanostructure of $BiVO_4$, CoBTC cannot fully cover its surface. Large resistance inhibits charge transfer across the interface between CoBTC and BVO, so the additional R–C pair is required. The highest CPE-P values of (CoBTC)-BVO imply the resulting charge accumulation and slow charge transfer at both BVO/cocatalyst interface and cocatalyst/electrolyte interface (Fig. 4(a)). What's more, due to long diffusion distance of the thick CoBTC cocatalyst layer, the photogenerated holes are more likely to recombine with electrons before reaching the surface for reaction, which is indicated by the largest $R_{ct,1}$ of (CoBTC)-BVO. By contrast, in Co-BTC-BVO and Co-BVO, chemical bonds at the interface and the molecular-level thickness are beneficial to charge transfer without severe accumulation.

On the other hand, Co-BVO photoanodes possess moderate performance that is also lower than that of Co-BTC-BVO. EIS spectra in Fig. 5(d) imply that the BTC molecules can greatly improve charge transfer between Co^{2+} and BVO. As given in Table S6 in the ESM, the value of interfacial charge transfer resistance R_{ct} of Co-BTC-BVO is about 10.851 kΩ, much smaller than that of Co-BVO (100.24 kΩ). Charge transfer efficiencies calculated according to *J*–*V* curves in the electrolytes without and with hole scavenger (Fig. S15 in the ESM) are shown in Fig. 5(g). Co-BTC-BVO exhibits a high charge transfer efficiency of 91.9% at 1.23 V_{RHE}.

Stability test at 0.8 V_{RHE} (Fig. S16 in the ESM) demonstrates that the photocurrent density of (CoBTC)-BVO decays rapidly in 15 min, possibly resulting from the drop of CoBTC nanoparticles. The gradual decrease of photocurrent of Co-BTC-BVO and Co-BVO may result from the dissolution of surface Co^{2+} species. As shown in Fig. S17 in the ESM, after 3 h test, the intensity of high-resolution XPS Co peaks is apparently weakened. However, Co-BTC-BVO exhibits better stability than Co-BVO, therefore the BTC molecules not only bind between Co^{2+} and BVO as a bridge for charge transfer, but also tightly chelate with Co^{2+} to improve the stability.

3 Conclusions

In summary, we demonstrated the feasibility of an organic ligand, BTC, as a passivation layer for BVO photoanodes, as well as anchor for a molecular cocatalyst. Detailed investigations revealed that BTC forms strong coordination with Bi atoms and modulates surrounding electron distribution. After adding Co^{2+} ions, a molecular cocatalyst forms, and the charge transfer efficiency can also be promoted to over 90%. By taking advantage of the chemical bonding between the functional groups of BTC, BVO, and surface Co^{2+}, the Co-BTC-BVO photoanode exhibits an excellent photocurrent of 4.82 mA/cm^2 at 1.23 V_{RHE} and a low onset potential of 0.22 V_{RHE} under AM 1.5 G illumination. Compared to bulk cocatalyst, the molecular cocatalyst Co-BTC possesses more conformal coverage and higher OER activity due to more favorable charge kinetics. Our results emphasize the significance of interfacial chemical bonding for charge transfer. The strategy developed here may provide a novel selection for photoanode surface passivation and cocatalyst loading for photoelectrochemical water splitting with outstanding performance.

4 Experimental section

4.1 Materials

$Bi(NO_3)_3{\cdot}5H_2O$ (99%, analytial reagent (AR)), methanol (99.5%, AR), and $Co(NO_3)_2{\cdot}6H_2O$ (99%, AR) were purchased from Sinopharm Chemical Reagent Co., Ltd. KI (99%, AR), ethanol (99.5%, AR), p-benzoquinone (98%, chemically pure (CP)), dimethyl sulfoxide (99.5%, AR), vanadyl acetylacetonate (99%, AR), NaOH (96%, AR), *N*,*N*-dimethylformamide (99.5%, AR), and 1,3,5-benzenetricarboxylic acid (99%, AR) were purchased from Shanghai Aladdin Biochemical Technology Co., Ltd. All chemicals were used without further purification.

4.2 Preparation of BVO electrodes

Before synthesis, the fluorine-doped tin oxide (FTO) pieces were ultrasonic cleaned in water, acetone, and ethanol in sequence for 20 min. The electrodeposition process was carried out according to Ref. [21] with the electrodeposition of BiOI and subsequent calcination with vanadyl acetylacetonate ($VO(acac)_2$).

4.3 Preparation of BTC-BVO, Co-BTC-BVO, Co-BVO, and (CoBTC)-BVO electrodes

For BTC-BVO electrodes, 0.05 M BTC was dissolved into 15 mL of DMF and 5 mL of methanol, stirred for 30 min, and transferred to a 50-mL Teflon-lined stainless-steel autoclave. A piece of BVO electrode was put into the autoclave. The solvothermal reaction was held at 120 °C for 20 h. The obtained BTC-BVO electrode was rinsed by deionized (D.I.) water and dried in the air.

Co-BTC-BVO and Co-BVO electrodes were obtained by immersing BTC-BVO or BVO films into 10 mM $Co(NO_3)_2{\cdot}6H_2O$ solution for 10 min.

For (CoBTC)-BVO electrodes, 10 mM $Co(NO_3)_2{\cdot}6H_2O$ and 0.05 M BTC were dissolved into 15 mL of DMF and 5 mL of methanol. The subsequent solvothermal process was the same as that of BTC-BVO.

4.4 Photoelectrochemical measurement

All the PEC measurements were performed on an electrochemical workstation (CHI660E, CH Instruments, Inc.) using a three-electrode configuration with 1 M potassium borate solution (1 M KBi, pH = 9.7) as the electrolyte, unless otherwise noted. An Ag/AgCl (saturated KCl) electrode and a Pt foil were used as reference electrode and counter electrode. All the potentials reported versus RHE were converted from potentials vs. Ag/AgCl according to the following equation $E_{RHE} = E_{Ag/AgCl} + 0.059 \times pH + E^0_{Ag/AgCl}$ ($E^0_{Ag/AgCl} = 0.197$ V at 25 °C) [42]. A 300 W Xe lamp (CEL-HXUV300, CEAULIGHT Co. Ltd.) equipped with an AM 1.5 G filter was illuminated from the back side of the samples as the light source. The light intensity on the samples was adjusted to 100 mW/cm^2.

IMPS was performed using an electrochemical workstation

(Zahner Instrument, Germany) equipped with an illumination intensity-modulated photospectroscope that allowed the superimposition of sinusoidal modulation on DC illumination at varying potentials from 0.9 to 1.3 V_{RHE}. The modulation frequency ranged from 0.1 Hz to 100 kHz, and the illumination intensity was set at 100 mW/cm^2. The gas evolution of H_2 and O_2 was measured by a gas chromatograph (Shimadzu GC-2014C) in an air-tight cell at 0.8 V_{RHE} under AM 1.5 G illumination.

4.5 Material characterization

The morphology of the electrodes was characterized by SEM (JSM-6360LV) and TEM (Talos F200X G2). The crystalline structures of the samples were recorded on a Rigaku D/max 2550VL/PC system, using Cu Kα radiation. Raman spectra were recorded at room temperature using a Renishaw inVia spectrometer. A 532 nm He-Ne laser was used as the excitation source. FTIR spectra were obtained by a Thermo Scientific Nicolet 6700 spectrometer. UV–Vis absorption spectra were measured by a PerkinElmer Lambda 750S UV–Vis–NIR (NIR: near infrared) spectrophotometer. XPS spectra were collected on a Thermo Scientific Kα X-ray photoelectron spectrometer with an Al Kα ($h\nu$ = 1486.6 eV) radiation source. All the binding energy was referred to the C 1s peak (284.8 eV) from adventitious carbon. PL spectra were acquired at room temperature on a Shimadzu RF-5301PC fluorescence spectrophotometer with an excitation wavelength of 400 nm. The TRPL test was carried out on an Edinburgh Instruments FLS1000 Fluorescence Spectrofluorometer. The average lifetimes of different photoanodes were calculated as $\langle\tau\rangle = (A_1\tau_1^2 + A_2\tau_2^2)/(A_1\tau_1 + A_2\tau_2)$ [13].

4.6 Computational details

All the calculations were conducted by DFT methods in the Vienna *ab initio* simulation package (VASP) [43]. The generalized gradient approximation (GGA) of the Perdew–Burke–Ernzerhof (PBE) functional was applied to describe the exchange-correlation potential. The energy cutoff for plane-wave expansion was 400 eV. The geometry configurations were optimized by the convergence criteria of 1×10^{-4} eV and 0.05 eV/Å for the electronic energy and force. The vacuum space was set to be 30 Å to avoid interactions between periodic slabs. $BiVO_4$ slab was established by cutting the (001) surface of bulk $BiVO_4$, which contains 96 atoms. In the calculations, the electronic spin polarization was always considered, and all calculations were performed at the Γ-point. The charge difference was calculated using package VASPKIT [44].

Acknowledgements

The authors kindly acknowledge the financial support from the National Natural Science Foundation of China (No. 51672173, U1733130); Shanghai Science and Technology Committee (Nos. 21ZR1435700, 18520744700, and 18JC1410500); and Shanghai Jiao Tong University Medical Engineering Cross Research Program (No. YG2023ZD18). The computations in this paper were run on the Siyuan-1 cluster supported by the Center for High Performance Computing at Shanghai Jiao Tong University.

Electronic Supplementary Material: Supplementary material (electrochemical calculation methods, Raman spectra, SEM image, XPS spectra, 3D charge density difference, ABPE, UV–Vis spectra, Tauc plots, M–S plots, open-circuit potential, IMPS curves, EIS curves, and stability performance) is available in the online version of this article at https://www.doi.org/10.1007/s12274-023-6262-1.

References

[1] Sivula, K.; van de Krol, R. Semiconducting materials for photoelectrochemical energy conversion. *Nat. Rev. Mater.* **2016**, *1*, 15010.

[2] Jiang, C. R.; Moniz, S. J. A.; Wang, A. Q.; Zhang, T.; Tang, J. W. Photoelectrochemical devices for solar water splitting-materials and challenges. *Chem. Soc. Rev.* **2017**, *46*, 4645–4660.

[3] Grätzel, M. Photoelectrochemical cells. *Nature* **2001**, *414*, 338–344.

[4] Trześniewski, B. J.; Smith, W. A. Photocharged $BiVO_4$ photoanodes for improved solar water splitting. *J. Mater. Chem. A* **2016**, *4*, 2919–2926.

[5] Kan, M.; Xue, D. Q.; Jia, A. H.; Qian, X. F.; Yue, D. T.; Jia, J. P.; Zhao, Y. X. A highly efficient nanoporous $BiVO_4$ photoelectrode with enhanced interface charge transfer Co-catalyzed by molecular catalyst. *Appl. Catal. B* **2018**, *225*, 504–511.

[6] Li, X.; Liu, S. W.; Fan, K.; Liu, Z. Q.; Song, B.; Yu, J. G. MOF-based transparent passivation layer modified ZnO nanorod arrays for enhanced photo-electrochemical water splitting. *Adv. Energy Mater.* **2018**, *8*, 1800101.

[7] Li, D. Y.; Huang, Y. L.; Ma, R. J.; Liu, H.; Liang, Q.; Han, Y.; Ren, Z. W.; Liu, K.; Fong, P. W. K.; Zhang, Z. Q. et al. Surface regulation with polymerized small molecular acceptor towards efficient inverted perovskite solar cells. *Adv. Energy Mater.* **2023**, *13*, 2204247.

[8] Mao, L. L.; Huang, Y. C.; Deng, H.; Meng, F. Q.; Fu, Y. M.; Wang, Y. Q.; Li, M. T.; Zhang, Q. H.; Dong, C. L.; Gu, L. et al. Synergy of ultrathin CoO_x overlayer and nickel single atoms on hematite nanorods for efficient photo-electrochemical water splitting. *Small* **2023**, *19*, 2203838.

[9] Zhang, S. C.; Liu, Z. F.; Chen, D.; Yan, W. G. An efficient hole transfer pathway on hematite integrated by ultrathin Al_2O_3 interlayer and novel $CuCoO_x$ cocatalyst for efficient photoelectrochemical water oxidation. *Appl. Catal. B* **2020**, *277*, 119197.

[10] Fu, S. R.; Hu, H. Y.; Feng, C. C.; Zhang, Y. J.; Bi, Y. P. Epitaxial growth of $ZnWO_4$ hole-storage nanolayers on ZnO photoanodes for efficient solar water splitting. *J. Mater. Chem. A* **2019**, *7*, 2513–2517.

[11] Ning, X. M.; Du, P. Y.; Han, Z. G.; Chen, J.; Lu, X. Q. Insight into the transition-metal hydroxide cover layer for enhancing photoelectrochemical water oxidation. *Angew. Chem., Int. Edit.* **2021**, *60*, 3504–3509.

[12] Usman, E.; Vishlaghi, M. B.; Kahraman, A.; Solati, N.; Kaya, S. Modifying the electron-trapping process at the $BiVO_4$ surface states via the TiO_2 overlayer for enhanced water oxidation. *ACS Appl. Mater. Interfaces* **2021**, *13*, 60602–60611.

[13] Varadhan, P.; Fu, H. C.; Priante, D.; Retamal, J. R. D.; Zhao, C.; Ebaid, M.; Ng, T. K.; Ajia, I.; Mitra, S.; Roqan, I. S. et al. Surface passivation of GaN nanowires for enhanced photoelectrochemical water-splitting. *Nano Lett.* **2017**, *17*, 1520–1528.

[14] Li, F.; Jian, J.; Xu, Y. X.; Liu, W.; Ye, Q.; Feng, F.; Li, C.; Jia, L. C.; Wang, H. Q. Surface defect passivation of Ta_3N_5 photoanode via pyridine grafting for enhanced photoelectrochemical performance. *J. Chem. Phys.* **2020**, *153*, 024705.

[15] Firet, N. J.; Venugopal, A.; Blommaert, M. A.; Cavallari, C.; Sahle, C. J.; Longo, A.; Smith, W. A. Chemisorption of anionic species from the electrolyte alters the surface electronic structure and composition of photocharged $BiVO_4$. *Chem. Mater.* **2019**, *31*, 7453–7462.

[16] Köppen, M.; Dhakshinamoorthy, A.; Inge, A. K.; Cheung, O.; Ångström, J.; Mayer, P.; Stock, N. Synthesis, transformation, catalysis, and gas sorption investigations on the bismuth metal-organic framework CAU-17. *Eur. J. Inorg. Chem.* **2018**, *2018*, 3496–3503.

[17] Zhang, R. Q.; Liu, Y. Y.; Wang, Z. Y.; Wang, P.; Zheng, Z. K.; Qin, X. Y.; Zhang, X. Y.; Dai, Y.; Whangbo, M. H.; Huang, B. B. Selective photocatalytic conversion of alcohol to aldehydes by singlet oxygen over Bi-based metal-organic frameworks under UV–vis light irradiation. *Appl. Catal. B* **2019**, *254*, 463–470.

[18] Ying, Y. L.; Khezri, B.; Kosina, J.; Pumera, M. Reconstructed

bismuth-based metal-organic framework nanofibers for selective CO_2-to-formate conversion: Morphology engineering. *ChemSusChem* **2021**, *14*, 3402–3412.

[19] Zhang, Y. J.; Xu, L. C.; Liu, B. Y.; Wang, X.; Wang, T. S.; Xiao, X.; Wang, S. C.; Huang, W. Engineering $BiVO_4$ and oxygen evolution cocatalyst interfaces with rapid hole extraction for photoelectrochemical water splitting. *ACS Catal.* **2023**, *13*, 5938–5948.

[20] Li, F. S.; Yang, H.; Zhuo, Q. M.; Zhou, D. H.; Wu, X. J.; Zhang, P. L.; Yao, Z. Y.; Sun, L. C. A cobalt@cucurbit[5]uril complex as a highly efficient supramolecular catalyst for electrochemical and photoelectrochemical water splitting. *Angew. Chem., Int. Ed.* **2021**, *60*, 1976–1985.

[21] Kim, T. W.; Choi, K. S. Nanoporous $BiVO_4$ photoanodes with dual-layer oxygen evolution catalysts for solar water splitting. *Science* **2014**, *343*, 990–994.

[22] Yao, D. Z.; Tang, C.; Vasileff, A.; Zhi, X.; Jiao, Y.; Qiao, S. Z. The controllable reconstruction of Bi-MOFs for electrochemical CO_2 reduction through electrolyte and potential mediation. *Angew. Chem., Int. Ed.* **2021**, *60*, 18178–18184.

[23] Pan, J. B.; Wang, B. H.; Wang, J. B.; Ding, H. Z.; Zhou, W.; Liu, X.; Zhang, J. R.; Shen, S.; Guo, J. K.; Chen, L. et al. Activity and stability boosting of an oxygen-vacancy-rich $BiVO_4$ photoanode by NiFe-MOFs thin layer for water oxidation. *Angew. Chem., Int. Ed.* **2021**, *60*, 1433–1440.

[24] Lin, J. Y.; Han, X. J.; Liu, S. Y.; Lv, Y.; Li, X.; Zhao, Y. X.; Li, Y.; Wang, L. Z.; Zhu, S. M. Nitrogen-doped cobalt-iron oxide cocatalyst boosting photoelectrochemical water splitting of $BiVO_4$ photoanodes. *Appl. Catal. B* **2023**, *320*, 121947.

[25] Zhu, S. M.; Yan, D. Y. Atom transfer radical polymerization of methyl methacrylate catalyzed by $Iron^{II}$ chloride/isophthalic acid system. *Macromolecules* **2000**, *33*, 8233–8238.

[26] Xie, J. L.; Guo, C. X.; Yang, P. P.; Wang, X. D.; Liu, D. Y.; Li, C. M. Bi-functional ferroelectric $BiFeO_3$ passivated $BiVO_4$ photoanode for efficient and stable solar water oxidation. *Nano Energy* **2017**, *31*, 28–36.

[27] Lu, Y. M.; Su, J. Z.; Shi, J. W.; Zhou, D. Surface recombination passivation of the $BiVO_4$ photoanode by the synergistic effect of the cobalt/nickel sulfide cocatalyst. *ACS Appl. Energy Mater.* **2020**, *3*, 9089–9097.

[28] Wang, S. C.; He, T. W.; Chen, P.; Du, A. J.; Ostrikov, K.; Huang, W.; Wang, L. Z. *In situ* formation of oxygen vacancies achieving near-complete charge separation in planar $BiVO_4$ photoanodes. *Adv. Mater.* **2020**, *32*, 2001385.

[29] Prabhakar, R. R.; Moehl, T.; Friedrich, D.; Kunst, M.; Shukla, S.; Adeleye, D.; Damle, V. H.; Siol, S.; Cui, W.; Gouda, L. et al. Sulfur treatment passivates bulk defects in Sb_2Se_3 photocathodes for water splitting. *Adv. Funct. Mater.* **2022**, *32*, 2112184.

[30] Zhang, M. Y.; Antony, R. P.; Chiam, S. Y.; Abdi, F. F.; Wong, L. H. Understanding the roles of NiO_x in enhancing the photoelectrochemical performance of $BiVO_4$ photoanodes for solar water splitting. *ChemSusChem* **2019**, *12*, 2022–2028.

[31] Sun, Q.; Cheng, T.; Liu, Z. R.; Qi, L. M. A cobalt silicate modified $BiVO_4$ photoanode for efficient solar water oxidation. *Appl. Catal. B* **2020**, *277*, 119189.

[32] Dai, Y. W.; Cheng, P.; Xie, G. C.; Li, C. C.; Akram, M. Z.; Guo, B. D.; Boddula, R.; Shi, X. H.; Gong, J. L.; Gong, J. R. Modulating photoelectrochemical water-splitting activity by charge-storage capacity of electrocatalysts. *J. Phys. Chem. C* **2019**, *123*, 28753–28762.

[33] Li, Y.; Dai, X. Y.; Bu, Y. Y.; Zhang, H. Z.; Liu, J.; Yuan, W. Y.; Guo, X. H.; Ao, J. P. Photoelectrochemical performance improving mechanism: Hybridization appearing at the energy band of $BiVO_4$ photoanode by doped quantum layers modification. *Small* **2022**, *18*, 2200454.

[34] Liu, Z. Y.; Wu, X. F.; Zheng, B. N.; Sun, Y.; Hou, C. M.; Wu, J.; Huang, K. K.; Feng, S. H. Cobalt-plasma treatment enables structural reconstruction of a $CoO_x/BiVO_4$ composite for efficient photoelectrochemical water splitting. *Chem. Commun.* **2022**, *58*, 9890–9893.

[35] Wang, S. C.; Chen, P.; Yun, J. H.; Hu, Y. X.; Wang, L. Z. An electrochemically treated $BiVO_4$ photoanode for efficient photoelectrochemical water splitting. *Angew. Chem., Int. Ed.* **2017**, *56*, 8500–8504.

[36] Walter, M. G.; Warren, E. L.; McKone, J. R.; Boettcher, S. W.; Mi, Q. X.; Santori, E. A.; Lewis, N. S. Solar water splitting cells. *Chem. Rev.* **2010**, *110*, 6446–6473.

[37] Klahr, B.; Gimenez, S.; Fabregat-Santiago, F.; Hamann, T.; Bisquert, J. Water oxidation at hematite photoelectrodes: The role of surface states. *J. Am. Chem. Soc.* **2012**, *134*, 4294–4302.

[38] Lopes, T.; Andrade, L.; Le Formal, F.; Gratzel, M.; Sivula, K.; Mendes, A. Hematite photoelectrodes for water splitting: Evaluation of the role of film thickness by impedance spectroscopy. *Phys. Chem. Chem. Phys.* **2014**, *16*, 16515–16523.

[39] Agarwal, P.; Orazem, M. E.; Garcia-Rubio, L. H. Measurement models for electrochemical impedance spectroscopy: I. *Demonstration of applicability*. *J. Electrochem. Soc.* **1992**, *139*, 1917–1927.

[40] Abouzari, M. R. S.; Berkemeier, F.; Schmitz, G.; Wilmer, D. On the physical interpretation of constant phase elements. *Solid State Ionics* **2009**, *180*, 922–927.

[41] Chang, S. H.; Liou, J. S.; Liu, J. L.; Chiu, Y. F.; Xu, C. H.; Chen, B. Y.; Chen, J. Z. Feasibility study of surface-modified carbon cloth electrodes using atmospheric pressure plasma jets for microbial fuel cells. *J. Power Sources* **2016**, *336*, 99–106.

[42] Wang, S. C.; He, T. W.; Yun, J. H.; Hu, Y. X.; Xiao, M.; Du, A. J.; Wang, L. Z. New iron-cobalt oxide catalysts promoting $BiVO_4$ films for photoelectrochemical water splitting. *Adv. Funct. Mater.* **2018**, *28*, 1802685.

[43] Kresse, G.; Furthmuller, J. Efficient iterative schemes for *Ab initio* total-energy calculations using a plane-wave basis set. *Phys. Rev. B* **1996**, *54*, 11169–11186.

[44] Wang, V.; Xu, N.; Liu, J. C.; Tang, G.; Geng, W. T. VASPKIT: A user-friendly interface facilitating high-throughput computing and analysis using VASP code. *Comput. Phys. Commun.* **2021**, *267*, 108033.